A System for Probing Casimir Energy Corrections to the Condensation Energy

Diego Pérez-Morelo[1,2,3], Alexander Stange[4], Richard W. Lally[4], Lawrence K. Barrett[4], Matthias Imboden[6], Abhishek Som[5], David K. Campbell[1,4,5], Vladimir A. Aksyuk[2] and David J. Bishop[1,4,5,7,8]

1. *Department of ECE, Boston University, Boston, MA 02215*
2. *Physical Measurement Laboratory, National Institute of Standards and Technology, Gaithersburg, MD 20899*
3. *Institute for Research in Electronics and Applied Physics & Maryland NanoCenter, University of Maryland, College Park, MD 20742*
4. *Division of MSE, Boston University, Boston, MA 02215*
5. *Department of Physics, Boston University, Boston, MA 02215*
6. *Institute of Microengineering, École Polytechnique Fédérale de Lausanne (EPFL), Neuchâtel, Switzerland*
7. *Department of ME, Boston University, Boston, MA 02215*
8. *Department of BME, Boston University, Boston, MA 02215*

Contact email addresses:
DPM: djperez@umd.edu
AS: stange@bu.edu
RWL: rlally@bu.edu
LKB: blawrenc@bu.edu
MI: mimboden@bu.edu
AS: asom5@bu.edu
DKC: dkcampbe@bu.edu
VAK: vladimir.aksyuk@nist.gov

Corresponding author:
David J. Bishop: djb1@bu.edu
8 St. Mary's St, Room 609
Boston, MA 02215
(617) 353-8899

Abstract

In this article, we present a nanoelectromechanical system (NEMS) designed to detect changes in the Casimir energy. The Casimir effect is a result of the appearance of quantum fluctuations in an electromagnetic vacuum. Previous experiments have used nano- or microscale parallel plate capacitors to detect the Casimir force by measuring the small attractive force these fluctuations exert between the two surfaces. In this new set of experiments, we aim to directly detect the shifts in the Casimir *energy* in vacuum due to the presence of the metallic parallel plates, one of which is a superconductor. A change in the Casimir energy of this configuration is predicted to shift the superconducting transition temperature (T_c) because of the interaction between it and the superconducting condensation energy. In our experiment, we take a superconducting film, carefully measure its transition temperature, bring a conducting plate close to the film, create a Casimir cavity, and then measure the transition temperature again. The expected shifts are smaller than the normal shifts one sees in cycling superconducting films to cryogenic temperatures, so using a NEMS resonator *in situ* is the only practical way to obtain accurate, reproducible data. Using a thin Pb film and opposing Au surface, we observe no shift in T_c greater than 12 μK down to a minimum spacing of approximately 70 nm at zero applied magnetic field.

INTRODUCTION

The Casimir force was first derived in 1948 by calculating the van der Waals force using retarded potentials [1]. This force is a purely quantum mechanical force that arises between two plates even when they are not electrically charged. Classically, there is no force on the plates. However, due to quantum fluctuations and the freezing out of the long-wavelength electromagnetic modes, there is a net pressure exerting an attractive force. Experimentally, the effect has been seen using a number of microscale systems and devices [2-8]. Ref. [4] discusses how the force varies with the metallic conductivity of the plates, Refs. [9] and [10] show how the effect can be used for practical applications and [11], [12] show how a repulsive force can be achieved. Additional work has also demonstrated the importance of nanopatterning [13] and magnetic effects [14].

Given that the metallic conductivity changes the magnitude of the Casimir force, the question immediately comes to mind "what happens if the plates become superconducting?" The answer disappointingly is "not much." The Casimir effect averages the conductivity of the material over very large energy scales, while the superconducting gap is relevant only for the far infrared [15]. Therefore, while the effect of superconductivity is very large (100 %) on the DC conductivity, it is negligible and unmeasurable if averaged over the typical energy scales found in a Casimir cavity [16]. Therefore, one cannot see an effect on the measured Casimir force at the transition temperature T_c.

However, as pointed out in work by Bimonte and coworkers [17], one might be able to see an effect of Casimir *energy* on the superconductivity. In a type I superconductor, the critical parallel field $H_{c||}(T)$ is given by the change in the free energy, ΔF, which is the difference between the free energy in the superconducting and normal states:

$$(H_{c||}(T))^2 \propto \Delta F(T) \qquad (1)$$

Ref. [17] suggests that this free energy change may also be related to the Casimir energy:

$$\Delta F = E_{cond}(T) + \Delta E_{Cas}(T) \qquad (2)$$

where $E_{cond}(T)$ is due to the superconductivity and $\Delta E_{Cas}(T)$ is due to the Casimir energy. For small modulations in this Casimir term, the critical field is modulated by a factor proportional to the ratio $\Delta E_{Cas}/E_{cond}$. The calculations performed in Ref. [18] suggest that this fraction could be as large as 10 % in certain thin film materials with low condensation energies.

The theory suggests the following: First, placing a superconducting film in a Casimir cavity shifts T_c. Second, measuring the effect is contingent upon keeping E_{cond} constant. Therefore, any attempt to compare several different films, some inside cavities and some not, may suffer from uncertainty due to variations in the highly process-dependent characteristics of superconducting thin films. Even on a single die, different regions of the deposited material may display slightly different superconducting transition temperatures due to thickness variations, local roughness, or temperature gradients during deposition. In this work, we present a technique in which a nanoelectromechanical system (NEMS) structure is used to move a plate relative to a single superconducting film *in situ*. The basic concept is shown in Figure 1, in which we sit on the shoulder of the superconducting transition and actuate a nearby metallic plate, thus modulating the Casimir energy while monitoring the film resistance. Due to the sharp slope of the superconducting transition, a small change in T_c (due to a change in the Casimir energy) would manifest as a measurable change in the sample resistance. The present experimental approach can be extended to include the application of a magnetic field through the sample, allowing one to measure variations in the full $H_c(T)$ curve for comparison with the existing theory, which currently does not provide quantitative predictions for $H = 0$ [17,18].

There are a number of experimental challenges posed by the concept shown in Figure 1. According to calculations performed in Refs. [17] and [18], the spacing of the Casimir cavity should be in the range of a few nanometers to 100 nm, and the film thickness should be on the order of 10 nm. These characteristics place serious constraints on the choice of materials, many of which tend to ball up and form islanded microstructures when thin [19]. However, evaporating onto cryogenically cooled surfaces allows for the quenched condensation of the material, forming very smooth, amorphous films [20, 21]. For this reason, an *in situ* deposition method is used in which the superconducting film is deposited at the chip scale, below the superconducting transition temperature. This "fab-on-a-chip" methodology is explained further in the Methods section as well as in Refs. [21-25]. It is with this quenched-condensed thin film (which serves as one half of a tunable Casimir cavity) that we are able to probe changes in the Casimir energy.

RESULTS

Experiments are performed by assembling a target chip and a source chip into a single package. Then, the system is cooled down to cryogenic temperatures, a superconducting thin film is deposited onto the target die, and a Casimir cavity is formed. Next, the film is characterized, and the size of the Casimir cavity is dynamically tuned while monitoring the film resistance. The *ex situ* characterization of the film and cavity is also performed using scanning electron microscopy (SEM) and atomic force microscopy (AFM) after the experiment is complete. The following results are presented according to this sequence.

Chip-scale evaporation and measurement setup

The nonrigid Casimir cavity imposes serious nanofabrication challenges that must be overcome to successfully obtain a functional device. First, due to process incompatibilities, we need to be able to deposit the superconducting sample underneath the metallic plate after releasing the movable structures. Second, due to the oxidation of the thin film, evaporation and resistance measurements need to be performed without breaking vacuum conditions. Finally, low temperatures can be used to reduce the migration of the evaporated material along the substrate, enabling high-quality films.

Figure 2 shows a schematic of the three-die arrangement developed for this experiment, consisting of one NEMS target die (onto which the material will be evaporated) centered between two microsource dies. The flux of the material being evaporated diagonally from each microsource die will reach the target die and form a continuous, thin film underneath the top Au layer. This top Au layer on the target die serves as both a physical mask and a movable plate (to vary the Casimir gap size, which is nominally g_0). The bottom Au layer of the target die consists of two sets of electrical leads. The rectangular structures shown in Figure 2 (target schematic) are the plate drive and sense electrodes for the movable gold plate, with a ground shield around them. The four leads heading off at 45° (P1, P2, P3, P4) in the target die schematic are the four-point contacts to the superconducting film used to measure its resistance. The film is formed by two angular evaporations through the holes (red) that combine to form a continuous strip along the center. Another important feature of the target die is the presence of silicon oxide pillars that serve as physical stops for the movable Au plate, both protecting the sample from contact with the Au as well as providing information regarding the minimum cavity size achieved. The microsource dies, shown in purple, are separated by distance $d_{sources}$ and consist of an array of microscale heaters preloaded with a layer of superconducting material. The design and fabrication of the microsources and targets are explained further in the Supplementary Information.

Quenched-condensed Pb thin film

After the system is cooled to ≈ 3 K, the microsources are slowly heated until the evaporation of Pb occurs. By applying short voltage pulses through microsources, very small amounts of material can be evaporated in a controlled manner. Because the target die is cooled to cryogenic temperatures, the Pb reaching the target forms a quenched-condensed film of just 20 nm to 30 nm (see *ex situ* AFM results). According to the mask pattern displayed in Figure 2, the dual-angle deposited Pb film connecting four Au measurements leads to an 'H' pattern, allowing for a four-point resistance measurement to be made.

The measured resistance of the quenched-condensed Pb film as the temperature is swept from 4 K to 9.5 K and back down is shown in Figure 3. The temperature at which the film begins to condense into the superconducting phase is ≈ 7.05 K, just under the bulk value of 7.193 K [26], indicating a thicker film (approximately 20 nm [21]). The resistance of the film above T_c is ≈ 3.4 kΩ, and the slope at the center of the transition is (11.4 ± 0.4) kΩ/K. The uncertainty on the slope is reported from the 95 % confidence bounds of the linear fitting in the range of 6.75 K to 6.95 K.

Cavity modulation and T_c shift measurement

The experiment is carried out by setting the temperature of the cryostat to the steepest point of the transition (T ≈ 6.88 K), where the measured resistance is most sensitive to changes in temperature. Then, the plate drive voltage is swept through its mechanical resonance while measuring the modulation of the resistance of the sample at the mechanical motion frequency. By operating the NEMS around resonance, we can not only produce large changes in the gap size but also perform the measurement at a high frequency (> 1 MHz), which greatly reduces measurement noise. Plotted in Figure 4 are three trials using this detection method, Trial #1, Trial #2, and Trial #3. The black data points show the frequency dependence of the amplitude and phase of the Au plate (left and right figures, respectively). A common Duffing-nonlinear oscillator response is evident for amplitudes below the plate mechanical contact with the oxide pillars. The blue data points show the change in resistance of the sample expressed in units of change in the transition temperature, using the slope calculated in Figure 3.

The abscissa of the plots in Figure 4 is the frequency of the signal being applied at the drive electrode. Because this is a purely AC signal, the electrostatic force applied to the plate and its resulting motion is actually at twice this frequency (see Methods section for details on this detection scheme). This 2x frequency difference between the electrical drive and the expected superconductor modulation signal largely eliminates any direct electrical crosstalk. For each trial, the frequency is swept upwards, and the plate amplitude/phase and sample resistance are all recorded simultaneously.

Additionally, the same three trials shown in Figure 4 are plotted in Figure 5 but are zoomed in to the region of interest (close to contact with the oxide pillars and just after the amplitude drop). In addition to plotting the data points, we include two sliding average curves to help visualize trends in the noisy data. These sliding averages take the mean of either one value or three values on either side of each data point (thin blue line and thick purple line, respectively).

Ex situ **characterization**

After running the experiment in the cryostat, the SEM and AFM measurements of the nanocavity (with the top Au surface removed) are performed. In Figure 6a, the features of the bottom Au layer depicted in Figure 2 are shown, consisting of two rectangular electrodes and four measurement leads. Additionally, the deposited Pb sample is visible, connecting all four leads and forming a continuous strip down the center. Figure 6b and 6c show the AFM height measurements of the sample and the oxide stops. The sample height is measured to vary between 20 nm and 30 nm. Using the SEM image, the length of the central portion of the sample is (20.1 ± 0.1) µm, and its width is (403 ± 57) nm. These values are obtained by averaging several measurements along the sample width and length, and the uncertainty is one standard deviation. The height of the oxide pillars is measured to be 160 ± 1 nm from averaging the heights of the 6 measured pillars shown in Figure 6b, and the uncertainty is one standard deviation.

Because the plate comes into contact with the oxide pillars, it is possible to estimate the vertical displacement of the center of the plate; however, to accomplish this, an assumption of the shape of the deformed Au must be made. The difficulty of this estimate is that the stress state of the suspended Au layer at cryogenic temperature is unknown. Using a series of finite element simulations, a likely range of the minimum Au/Pb spacing (i.e., when the amplitude of the plate is maximum) is estimated to be between 63 nm and 73 nm. Across the entire length of the sample, the average Au/Pb spacing at maximum amplitude is estimated to lie between 85 nm and 141 nm. This analysis is explained further in the Methods.

DISCUSSION

We have developed a platform based on a variable gap cavity including a Au nanoscale mechanical resonator and a high-quality quenched-condensed superconductor film, enabling the simultaneous electromechanical control of the nanometric gap between plates and the transport measurement of the superconducting film using a four-probe configuration. The high-frequency detection method presented makes use of the natural resonance of the plate to obtain the large modulations of the cavity size and allows for the phase sensitive detection of changes in the sample resistance due to the plate motion only.

Analysis of the results

In this set of experiments, the temperature of the cryostat is set to the steepest part of the superconducting transition ($T \approx 6.88$ K), and three long-duration sweeps are made driving the plate to resonance from low to high frequency until it abruptly loses amplitude due to its nonlinear resonant response. This nonlinearity is well described by a simple Duffing equation with spring stiffening due to the mechanics of the doubly clamped plate. More general descriptions that include the electrostatic driving, roughness, or Casimir force [27] are not required. An important feature in the plate response is the evidence in all three trials of a sudden clear deviation from the Duffing-nonlinear oscillator model in the amplitude and phase behavior occurring at approximately 811.2 kHz. This finding is due to the onset of the plate interacting with the oxide stops. Any additional nonlinearities in the plate mechanics due to deformation alone does not appear in this discontinuous manner but instead likely appears gradually. In addition, the amplitude is nearly fixed beyond this point, which is the further indication of contact. Upon contacting the pillars, the maximum peak displacement of the most deflected point on the plate centerline is estimated to be between 183 nm and 193 nm, resulting in a minimum Casimir cavity size of between 63 nm and 73 nm. Along the entire length of the superconducting sample and plate center, we estimate the average gap size at the closest approach to be between 85 nm and 141 nm. After the plate reaches its maximum amplitude at resonance (approximately 815 kHz), the plate amplitude abruptly drops to zero, and the undeflected Casimir cavity size returns to ≈ 256 nm. This jump is where we might expect to see more clearly a corresponding change in the sample resistance if there were indeed a dependence of the superconducting transition temperature on the cavity size; however, no such statistically significant correlation is observed.

Another feature of the high frequency ΔT measurements is seemingly random jumps of (300 to 400) μK. The cause of these instabilities is unknown; however, based on analyzing the three trials together, we do not believe they are related to the plate position. For example, in trial #1, we observe a large displacement at 820 kHz, which is well after the large plate oscillations have ceased. In trial #2, there is a large jump that is interestingly close to the minimum gap range, but a closer inspection of the data in Figure 5 shows that it lags the plate contact by 4 or 5 data points (corresponding to 6 to 7.5 minutes of time difference), which is thus highly unlikely to be the effect we are looking for. Finally, in trial #3, ΔT appears to be tracking the plate amplitude, but then after the oscillations jump down, the signal does not follow. While undesirable, it is reasonable to assume that these intermittent jumps did not obscure the correlation between the abrupt change in the plate amplitude and the sample measurement. Rather, it is the underlying stochastic noise, indicated by the spread of the data of the individual areas shown in the green boxes in Figure 4, which determines the experimental resolution.

To accurately quantify the uncertainty of the temperature measurement, we first consider this stochastic spread of the raw data as well as the uncertainty in the slope of the transition. For this value, we use the lower 95 % confidence bound of the slope (11 kΩ/K) to conservatively claim a resolution. Using one standard deviation from each dataset shown in the green areas of Figure 4, averaging these with a weight prescribed by the number of data points in each set, and dividing by the lower estimate of the slope, we calculate a one standard deviation per data point of 28 μK.

We look for the change in the critical temperature at the point of the abrupt change from a high amplitude vibration to the almost negligible vibration of the plate. At this jump, we quantify the change in the measured data by averaging 4 individual ΔT points immediately before and immediately after the jump and subtracting the averaged values. The average difference from the three experimental runs is (7 ± 12) μK. Thus, any effect of plate position on the transition temperature of the superconductor in our system is well below the one standard deviation statistical uncertainty of 12 μK.

Interpretation of the experiment

In all three trials, no clear correlation between the plate amplitude or position and transition temperature was observed above our measurement resolution of 28 μK, and from the three trials combined, no change in T_c was observed to exceed the one standard deviation uncertainty of 12 μK. There are a few reasons that may explain this null result. No observation of this effect may be due to one or more of the following: 1) geometrical limitations, 2) superconductor limitations, and 3) theoretical uncertainties.

In the first case, the device geometry may not allow for a sufficiently small cavity to clearly observe a shift. The minimum cavity size that we are able to reach with the current configuration is at best on the order of 70 nm. Although this brings us into a theoretically interesting range, it may not be small enough to produce a measurable shift with the current materials. The uncertainty in the exact gap size exists due to the uncertain stress in the structure near 7 K, which is expanded upon in the Methods section. Using a basic scaling law shown in equation 8 (derived from calculations performed in Ref. [18]), we estimate the relative change in the Casimir free energy between this minimum cavity size and the undeformed cavity size to be ≈ 400 %. Further optimization of the timed oxide undercut and geometric design may allow for smaller cavities, which increase the magnitude of the Casimir free energy compared to the condensation energy of the Pb film. Additionally, as discussed in the Methods, the resonant mode shape analysis of the Au plate indicates that there is likely some degree of bowing of the plate along the length of the sample at the time of the closest approach, reducing the parallelism of the Au and Pb surfaces and thus the overall Casimir interaction.

Regarding the superconducting film itself, there are certain key material properties to consider when conducting this type of experiment. First, a low T_c value is generally desired because the condensation energy scales $\propto T_c^{2.6}$ [28]. As discussed, it is the ratio of the Casimir free energy to the condensation energy that determines the magnitude of the shift in the critical field, so generally speaking, the lower T_c is, the better. In the case of the experiment presented here, Pb has a relatively high T_c value but was chosen for other experimental advantages. Future work may involve investigating lower T_c materials. Another important material property is the plasma frequency. Bimonte *et al*. showed that high plasma frequency materials can change the strength of the Casimir free energy term by almost one order of magnitude [18]. Many of the calculations in their work use Be, with a plasma frequency of approximately 18 eV, which is higher than Pb, with a value of approximately 8 eV [29]. This reduction in the reflectivity at higher frequencies may result in a Casimir energy contribution to the free energy of condensation that is too small to observe.

Finally, there is the question of what we expect theoretically in the limit of zero applied magnetic field. The calculation methods used in this low field limit are not possible due to the condensation energy and the change in the free energy becoming comparable [30]. It is therefore not exactly clear what one might expect in terms of the magnitude of the change in the critical temperature as a result of a Casimir energy variation. Our experiment shows that for our geometry, materials, and in the range of temperatures we can resolve, there is no observed effect. Most certainly, the next steps in this project will involve extending the experiment to include magnetic characterization and extending the existing theory to the H = 0 case [31].

CONCLUSIONS

We have developed a unique nanomechanical transducer-based measurement technique and have undertaken a careful series of experiments to directly measure the shifts in the Casimir energy by placing a superconducting Pb film in a cavity and tuning the gap, looking for effects on the superconducting transition temperature of the film. Our chip-scale system can deposit and measure a superconducting thin film while simultaneously actuating a nearby plate, forming a tunable Casimir cavity. The *in situ* deposition process is achieved with two arrays of MEMS heaters that have been preloaded with a thick film of Pb and can be pulsed at low temperature to evaporate small amounts of material. The thin film is produced by using a shadow mask to define a precise pattern of the evaporated Pb (incident on the mask from two sides) that connects the four metallic measurement leads and creates a thin section of Pb directly underneath the movable Au plate. By driving a current with two sets of leads and measuring the voltage drop with the other two, we can measure the resistance of Pb. We monitor this resistance as the Au plate is driven to its mechanical resonance and back to zero amplitude.

Using finite element analysis, we are able to estimate the deformed mode shape at resonance, which places the minimum separation of Pb and Au between 63 nm and 73 nm. We estimate that at this gap size, the presence of the Au plate may be expected to produce the relative changes in the Casimir free energy of the Pb film of 2x to 4x; however, a quantitative prediction for the corresponding change in T_C is a subject of ongoing theoretical work [31] and is not available at present. The results presented here, at zero applied magnetic field, indicate that there are no observed Casimir-induced changes in T_c greater than 12 μK. By opening a novel experimental window regarding the relationship between the Casimir energy and superconductivity, we hope this work will stimulate further experimental and theoretical developments.

METHODS

In situ film deposition and characterization

An experiment is performed in a closed cycle cryostat specially designed for low mechanical vibrations. A typical experiment is performed as follows: 1) The source and target are mounted opposite one another and cooled to ≈ 3 K in the closed cycle system, 2) at low temperatures, Pb is evaporated onto the substrate, producing a smooth, continuous superconducting film, 3) the resistance of the Pb film is measured across its transition and 4) the spacing of the Casimir cavity is modulated by applying an alternating voltage between the drive electrode and the suspended Au plate while the temperature of the system is held at the shoulder of the superconducting transition.

The resistance and transition of the Pb film is initially measured using a four-point configuration, shown schematically in Figure 3 (inset). An excitation current, $I_{ex,}$ is applied at lead I+ (in series with an external 1 MΩ resistor) and travels through the central portion of the sample to I-, which is grounded through a 1 kΩ resistor. A voltage difference is then measured between the other two leads, V+ and V-. I_{ex} is a low-frequency AC current of ≈ 5 nA at 37.7 Hz. The differential voltage measurement is measured using a lock-in amplifier, and the resistance of the sample is then V_{diff}/I_{ex}. The temperature of the system is slowly swept across the transition (both down and up), which provides the slope of the transition, dR_s/dT, as well as T_c.

Plate actuation and high frequency measurement

The dynamic detection scheme involves measuring V_{diff} at the same frequency the plate is moving. First, we set the cryostat temperature to just below $T_{c,}$ where the resistance measurement is the most sensitive to the changes in temperature. Next, if the position of the plate does indeed influence the sample resistance due to the Casimir effect, then we expect a small modulation of R_s at the plate frequency. Subsequently, the voltage difference measured is as follows:

$$V_{\mathrm{diff}} = I_{\mathrm{ex}} \cdot (R_{\mathrm{s},0} + \Delta R(t)) \qquad (3)$$

where $R_{s,0}$ is the nominal sample resistance and ΔR(t) is the small variation due to the plate. We can further breakdown ΔR:

$$\Delta \mathrm{R} = \underbrace{\frac{\partial R}{\partial T}}_{\text{transition slope}} \cdot \underbrace{\frac{\partial T}{\partial d}}_{\text{Casimir}} \cdot \underbrace{d(t)}_{\text{plate position}} \qquad (4)$$

The 'Casimir' term is the theorized change in T_c of the Pb sample due to the changing position of the plate, d(t). This change is what we intend to detect. Thus, if we consider only the component of V_{diff} at the plate frequency, with amplitude $|V_{diff}|_{plate}$, then we can rearrange equation ΔR to obtain the amplitude of this expected effect:

$$\left|\frac{\partial T}{\partial d}\right| = \frac{|V_{\mathrm{diff}}|_{\mathrm{plate}}}{|I_{\mathrm{ex}}(t)| \cdot \frac{\partial R}{\partial T} \cdot |d(t)|} \qquad (5)$$

In this case, a more complex detection circuit is required. In Figure 7, a high-frequency AC drive signal is used to actuate the plate at its resonance. The plate amplitude is detected at twice this drive frequency using LIA 1. Simultaneously, a current goes through the sample at a low frequency, while V_{diff} is being measured at the same frequency as the plate using LIA 2. The output of LIA 2 is then fed into LIA 3, which is locked into the low frequency of the excitation signal. The DC output of LIA 3 is then equal to the amplitude $|V_{diff}|_{plate}$. The inset table in Figure 7 reports nominal values of each parameter presented in the schematic.

Variation in the Casimir free energy due to plate motion

It is possible to estimate the relative variation in the Casimir free energy difference using the result from Ref. [18]:

$$\Delta E_{\mathrm{Cas}} \propto \frac{1}{1+\left(\frac{d}{d_0}\right)^{1.15}} \qquad (6)$$

where d is the separation between the superconductor and metal and d_0 is the nominal separation (≈ 256 nm in our experiment). It should be noted, however, that Ref. [18] approximates the relation shown in equation 6 using a system where T_c = 0.5 K, the superconductor thickness is 5 nm, and d_0 = 8.3 nm, which is different than the system presented here. Considering the relative change in ΔE_{Cas} to be $\delta E_{Cas} = \Delta E_{Cas}(d)/\Delta E_{Cas}(d_0)$ with d(t) changing sinusoidally at $\omega = 2\pi f_2$ with amplitude A, we find:

$$\delta E_{\mathrm{Cas}}(t, A) = \frac{2}{1+\left(\frac{d_0 + A\sin(\omega t)}{d_0}\right)^{1.15}} \qquad (7)$$

To a first approximation, we assume that $\delta E_{Cas}(t)$ varies $T_c(t)$ linearly. Because the phase sensitive detection used in the experiment only measures the time-averaged component of the signal at ω, we can approximate equation 7 by considering only the time averaged magnitude of the first harmonic term as a function of A. Numerically solving for the magnitude of the first Fourier coefficient of $\delta E_{Cas}(t,A)$ over the range A = 0 nm to A = 200 nm and using d_0 = 256 nm, we find that it can be well approximated by a third order polynomial:

$$|\delta E_{\mathrm{Cas}}| = c_1 A + c_2 A^3 \qquad (8)$$

where $c_1 = 0.0225\ \mathrm{nm}^{-1}$ and $c_2 = 5.905 \times 10^{-9}\ \mathrm{nm}^{-3}$. Using equation 8, we can then estimate the relative change in the Casimir free energy for a given plate amplitude. This estimate considers two parallel areas, separated by d. In reality, the interaction of the Au plate and Pb sample is not parallel, and the geometry is defined by the deformed shape of the plate. An exact analytical calculation of the Casimir interactions between general, nonparallel shapes is an open problem, which we do not address in this analysis. However, a study of how the plate might be deforming at its resonance is discussed in the following section.

Estimating the plate deflection and mode shape using finite element analysis

Determining the exact amplitude of the plate and therefore the Casimir gap size is challenging due to a significant change in the dynamics that occurs between room temperature and the cryogenic temperature. This behavior is demonstrated by a large change in the resonant frequency, from ≈ 700 kHz to ≈ 1.8 MHz between 300 K and 3 K, respectively, indicating the substantial tensile stress that occurs in the top Au layer due to thermal contraction of the Au relative to the substrate. By examining the behavior of the signal at the sense electrode, it is possible to determine when contact with the oxide pillars occurs; however, determining the distance between the Pb sample and the center of the plate (parallel to the Pb sample) requires knowledge of the deformed shape of the Au plate at its resonance.

Qualitatively, a Duffing response nonlinearity arises due to the dynamic increase in the tension of the vibrating Au plate, which slightly increases the mean resonance frequency with amplitude. However, because this change in the dynamic stress over an oscillation cycle is much smaller than the static stress, the mode shape is not much different than that of a linear, prestressed structure. Using a commercial finite element software package to calculate mechanical eigenmodes, three different initial stress cases are considered to place bounds on the distance at which the center of the plate deflects at resonance. The first case considers zero initial stress, and the second and third cases include two different values of a uniaxially applied initial stress (0.1 GPa and 0.26 GPa, respectively).

After a mode shape is obtained, it is scaled in amplitude (Z) until any part of the surface comes into contact with any of the oxide pillars, and then the profile parallel to the sample is extracted. In Figure 8a, the values of maximum separation, minimum separation, and average separation are reported as well as the two lengths: L_{10} and L_{25}, which are the lengths of the sample that are within 10 % and 25 %, respectively, of the minimum gap size.

Case 1: Although there is clearly evidence of significant initial stress in the movable Au layer, it is necessary to estimate the upper bound of the plate deflection by considering the zero stress case. Solving for the first eigenfrequency of the device geometry returns a value of 470 kHz, which is, as expected, well below the measured 1.8 MHz.

Case 2: Clearly, for the simulation to match the measured resonant frequency, a prestress must be applied. The reason for the two different stress cases 2 and 3 is that in the high stress limit, finite element analysis suggests that the fundamental mode and the second mode become near degenerate and mix due to the slight layout asymmetry in the center cut of the moving plate. This resulting high stress mode shape is essentially only one side of the cavity moving up and down, while the other side moves with a much smaller amplitude. Case 2 considers an intermediate stress case before this degeneracy is reached, and the shape of the fundamental mode still resembles that of the zero stress case. In this simulation, the uniaxial prestress is equal to 0.1 GPa, and the resulting resonant frequency is 1.12 MHz.

Case 3: In this simulation, the uniaxial prestress is increased until we reach a resonant frequency that matches the experiment (≈ 1.8 MHz). This stress is equal to 0.26 GPa and is generally consistent with the estimates from the differential thermal expansion. However, in this high stress condition, the mode shape is very asymmetric due to the mixing of the fundamental and the second modes. As a result, only one edge of the Au displaces enough to become close to the sample (see Figure 8b).

A full understanding of the exact shape of the Au plate at its resonance is not possible; however, by using the measured current amplitude from the experiment in conjunction with postexperimental finite element analysis, we can infer that the minimum separation of the Pb sample and the Au plate is likely between 63 nm and 73 nm and that the average separation across the length of the sample is likely between 85 nm and 141 nm. Using the estimated scaling dependence shown in equation 8, these deflections would produce relative changes in the Casimir free energy in the Pb sample between 415 % and 439 % (when considering only the area near the minimum gap) and between 260 % and 388 % when considering the average gap over the length of the sample.

Acknowledgments

The authors would like to thank Daron Westly, Mark D. Stiles, Ph.D., J. Alexander Little, Ph.D., and Marcelo Davanco, Ph.D. for reviewing this manuscript and offering many meaningful suggestions. Additional thanks to Fartash Yusefi for the collection of the AFM data. This work is supported in part by the Cooperative Research Agreement between the University of Maryland and the National Institute of Standards and Technology Center for Nanoscale Science and Technology, Award 70NANB10H193, through the University of Maryland. Additional support of this work is provided by the National Science Foundation under Grants EEC-1647837, ECCS-1708283, EEC-0812056, a SONY Faculty Innovation Award, and DARPA/AFRL through award FA8650-15-C-7545.

Conflict of Interests

The authors declare that they have no conflicts of interest.

Author contributions

The device design and experiments were conceived by DPM, VAK, and DJB. Target device fabrication was carried out by DPM. Microsource device design and preparation was conducted by DPM and AS with input from RL. Measurement techniques were developed by DPM, AS, MI, VAK and DJB with experiments performed by AS. The analysis of the data and finite element modeling was performed by AS with input from VAK and DPM. The manuscript was written by AS with input from DPM, VAK, LKB, MI, RL, A. Som, DKC, and DJB.

References

1. Casimir, H. B. “On the attraction between two perfectly conducting plates”. Proc. K. Ned. Akad. Wet. **51**(793), 150 (1948).

2. Lamoreaux, S. K. “Demonstration of the Casimir Force in the 0. 6 to 6 μm Range”. Physical Review Letters **78**(1), 5-8 (1997).
3. Mohideen, U., & Roy, A. “Precision measurement of the Casimir force from 0.1 to 0.9 μm”. Physical Review Letters **81**(21), 4549 (1998).
4. Chan, H. B., Aksyuk, V. A., Kleiman, R. N., Bishop, D. J., & Capasso, F. “Quantum mechanical actuation of microelectromechanical systems by the Casimir force”. Science **291** (5510), 1941-1944 (2001).
5. Chan, H. B., Aksyuk, V. A., Kleiman, R. N., Bishop, D. J., & Capasso, F. “Nonlinear micromechanical Casimir oscillator”. Physical Review Letters **87**, 211801 (2001).
6. Tang, L., Wang, M., Ng, C.Y., Nikolic, M, Chan, C.T., Rodriguez, A.W., and Chan, H.B. “Measurement of non-monotonic Casimir forces between silicon nanostructures,” Nature Photonics, **11**, 97-101 (2017).
7. Antezza, M, Chan, H. B., Guizal, B., Marachevsky, V. N., Messina, R., and Wang, M. “Giant Casimir Torque between Rotated Gratings and the θ=0 Anomaly” Phys. Rev. Lett. **124**, 013903 (2020).
8. Stange, A., Imboden, M., Javor, J., Barrett, L., and Bishop, D. J., “Building a Casimir Metrology Platform with a Commercial MEMS Sensor”, Microsystems and Nanoengineering **5(1)**, 14 (2019).
9. Jourdan, G., Lambrecht, A., Comin, F., & Chevrier, J. “Quantitative non-contact dynamic Casimir force measurements”. EPL (Europhysics Letters) **85**(3), 31001 (2009).
10. Imboden, M., Morrison, J., Campbell, D. and Bishop, D. “Design of a Casimir-Driven Parametric Amplifier”. J. Appl. Phys. 116, 134504 (2014).
11. Munday, J., Capasso, F. & Parsegian V. Measured long-range repulsive Casimir–Lifshitz forces. *Nature* **457,** 170–173 (2009).
12. Levin, M., McCauley, A.P., Rodriguez, A.W., Reid, M.T. H., and Johnson, S.G. Casimir Repulsion between Metallic Objects in Vacuum Phys. Rev. Lett. 105, 090403 (2010).
13. Intravaia, F., Koev, S., Jung, I., Talin, A., Davids, P., Decca, R., Aksyuk, V., Dalvit, D. and Lopez, D. “Strong Casimir force reduction through metallic surface nanostructuring”. Nature Communications **4**:2515 (2013).
14. Bimonte, G., Lopez, D. and Decca, R. “Isoelectronic Determination of the Thermal Casimir Force”. Phys. Rev. **B93**, 184434 (2016).
15. Glover, R.E., and Tinkham, M. “Conductivity of Superconducting Films for Photon Energies between 0.3 and 40 kT_c,” Physical Review, **108**, 243 (1957).
16. Norte, R.A., Forsch, M., Wallucks, A., Marinković, I., and Gröblacher, S. “Platform for Measurements of the Casimir Force between Two Superconductors.” Phys. Rev. Lett. **121**, 030405 (2018).
17. Bimonte, G., Calloni, E., Esposito, G., Milano, L. and Rosa, L. “Towards Measuring Variations of Casimir Energy by a Superconducting Cavity” Phys. Rev. Lett. **94**, 180402 (2005).

18. Bimonte, G., Calloni, E., Esposito, G., and Rosa, L. "Variations of Casimir energy from a superconducting transition." Nuclear Physics B, **726** (3): 441-463 (2005).
19. Neugebauer, C. A. and Webb, M. B. "Electrical conduction mechanism in ultrathin, evaporated metal films." Journal of Applied Physics, **33** (1), 74-82 (1962).
20. Ekinci, KL, and Valles Jr., JM. "Morphology of Quench Condensed Pb Films near the Insulator to Metal Transition" Phys. Rev. Lett. 82, 1518 (1999).
21. Imboden, M., Han, H., Stark, T., and Bishop, D., "Cryogenic Fab on a Chip Sticks the Landing". ACS Nano **11**(9), 20274-20285 (2017).
22. Imboden, M., Han, H., Chang, J., Pardo, F., Bolle, C., Lowell, E., and Bishop, D. "Atomic Calligraphy: The Direct Writing of Nanoscale Structures Using MEMS". Nano Letters **13**, 3379-3384 (2013).
23. Imboden, M., Han, H., Stark, T., Lowell, E., Chang, J., Pardo, F., Bolle, C., del Corro, P., and Bishop, D. "Building a Fab on a Chip". Nanoscale **6**, 5049-5062 (2014).
24. Imboden, M., and Bishop, D. "Top-down Nanomanufacturing", Physics Today **67**, 45-50 (2014).
25. Han, H., Imboden, M., Stark, T., Del Corro, P. G., Pardo, F., Bolle, C. A., Lally, R. W., and Bishop, D. J. "Programmable solid state atom sources for nanofabrication." Nanoscale, **7** (24), 10735-10744, (2015).
26. Franck, J.P. & Martin, D.L., "The Superconducting Transition Temperature of Lead." Canadian Journal of Physics, **39** (9), 1320-1329 (1961).
27. Broer, W., Waalkens, H., Svetovoy, V.B., Knoester, J., and Palasantzas, G., "Nonlinear Actuation Dynamics of Driven Casimir Oscillators with Rough Surfaces." Physical Review Applied, **4**, 054016, (2015).
28. Lewis, H. W. "Superconductivity and Electronic Specific Heat." Physical Review, **101** (3), 939-939 (1956).
29. Ordal, M. A., Bell, R. J., Alexander, R. W., Long, L. L., and Querry, M. R. "Optical properties of fourteen metals in the infrared and far infrared: Al, Co, Cu, Au, Fe, Pb, Mo, Ni, Pd, Pt, Ag, Ti, V, and W." Applied Optics, **24**, 4493, (1985).
30. Bimonte, G., Born, D., Calloni, E., Esposito, G., Huebner, U., Il'ichev, E., Rosa, L., Tafuri, and Vaglio, R. "Low noise cryogenic system for the measurement of the Casimir energy in rigid cavities." Journal of Physics A: Mathematical and Theoretical, **41** (16), 164023, (2008).
31. Som, A., Pérez-Morelo, D., Stange, A., Lally, R.W., Barrett, L.K., Imboden, M., Aksyuk, V. A., Bishop, D. J., and Campbell, D.K. On-going work. 2020.

Figure legends

Figure 1: Basic concept of our experiment. Holding the system at temperature T_{exp}, just below the transition, a conducting plate is actuated in close proximity to a superconductor to modulate the Casimir contribution to its total free energy change of condensation (ΔF), and thereby T_c. The two positions shown correspond to the maximum and minimum gap sizes due to an oscillation of the plate.

Figure 2: Schematic of the experimental setup and target die. Two MEMS-based microsources (purple) generate a flux of Pb atoms that is deposited onto a specially designed target die. Using angled evaporation through a suspended, patterned Au layer (a), a continuous film (e) is formed that connects the four prepositioned measurement leads (P1, P2, P3, P4). Au electrodes (b, c) are then used to actuate and sense the top suspended Au layer. Grounded guards (d) surround each electrode to minimize the current leakage and stray electric fields. As shown in the target schematic, the pattern etched into the top Au layer (red) acts as both the mask for evaporation and allows the suspended portion of the top Au layer to move, resulting in a tunable Casimir cavity. Silicon oxide pillars (f) serve as a physical stop for the movable Au plate.

Figure 3: Superconducting transition of the quenched-condensed Pb film. Data points (gray dots) are taken both sweeping up and down through the transition, and the black line is the smoothed average of these data points. The slope of the transition is calculated to be (11.4 ± 0.4) kΩ/K. INSET: four-point resistance detection scheme. The current is applied through an external resistance, and the voltage drop across the Pb sample is measured.

Figure 4: High-frequency detection of superconducting Pb film and cavity size. Black data are amplitude (left plots) and phase (right plots) of the movable plate for each trial, along with fits to a Duffing model with ω_0 = 805.4 kHz and Q ≈ 3500 (red lines). Uncertainties for the amplitude measurements are smaller than the symbol size. Phase uncertainties are one standard deviation uncertainties propagated from the measured statistical uncertainties in the x and y quadratures. Regions where the plate comes into contact with the oxide pillars are highlighted in pink. As the plate is swept through its resonance, the Pb resistance is recorded and scaled to units of the temperature change (blue data) using the slope of the superconducting transition. Note that ΔT = 0 μK is arbitrary from plot to plot. The green boxes indicate the regions of data that are used to quantify the one standard deviation uncertainty of the ΔT measurements (28 μK for each point).

Figure 5: A closer look at high frequency results. Only the regions before, during, and after contact are plotted. In addition to the data points, the sliding averages are plotted for better visualization. The one standard deviation uncertainty on ΔT measurements is 28 μK for each point.

Figure 6: *Ex situ* analysis of the cavity and film. **a.** SEM image of the cavity with the top Au layer removed using adhesive tape. A continuous Pb film can seem to connect the four Au leads. **b.** AFM measurement of the Pb sample and several oxide stops. The height data corresponding to the red profile are plotted in **c**.

Figure 7: High-frequency detection circuit. The cryostat is held at a constant temperature just below T_c on the slope of the transition. The high-frequency V_{drive} signal is applied to the drive electrode and swept at frequency f_2. The plate then feels an electrostatic force at frequency $2f_2$. The amplitude of the plate is monitored by measuring the AC current going through the sense electrode using a current-to-voltage amplifier and a lock-in referenced to $2f_2$ (LIA 1). The voltage drop across the Pb sample is also detected at $2f_2$. If there is any change in T_c due to the Casimir cavity size, then this is the frequency at which it would occur. Because the excitation current, I_{ex}, is alternating at f_1, the DC output of LIA 2 is fed into a third lock-in, LIA 3, which is referenced at f_1.

Figure 8: **a.** Results from the finite element analysis for gap sizes achieved along the length of the Pb sample (20 µm in length) upon contact between the deformed Au plate and the oxide pillars. With no actuation, the gap size is assumed to be 256 nm (sample thickness subtracted from oxide thickness). **b.** 3D representation of the gap size estimation using finite element results for case 3 (high uniaxial stress). In this case, the profile of the plate along the sample (blue line) is asymmetric and reaches much closer to the sample on one side compared to the other. This reduces the average gap size as well as L_{10} and L_{25}.

FIGURE 1

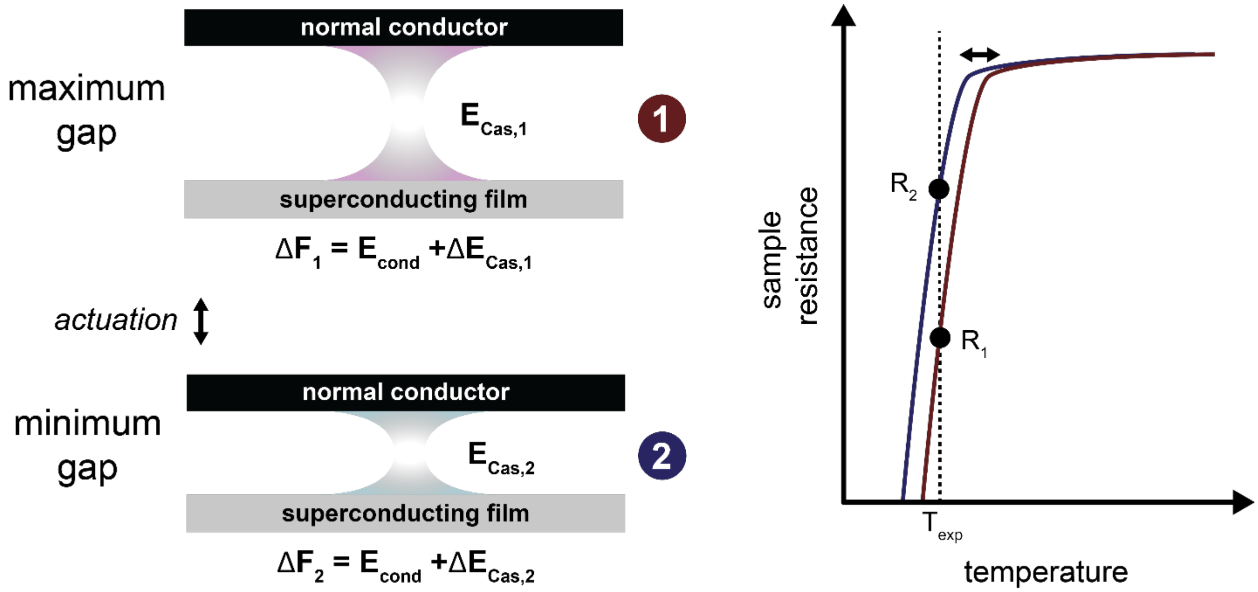
normal conductor
maximum gap
$E_{Cas,1}$
1
superconducting film
$\Delta F_1 = E_{cond} + \Delta E_{Cas,1}$
actuation
normal conductor
minimum gap
$E_{Cas,2}$
2
superconducting film
$\Delta F_2 = E_{cond} + \Delta E_{Cas,2}$
sample resistance
R_2
R_1
T_{exp}
temperature

FIGURE 2

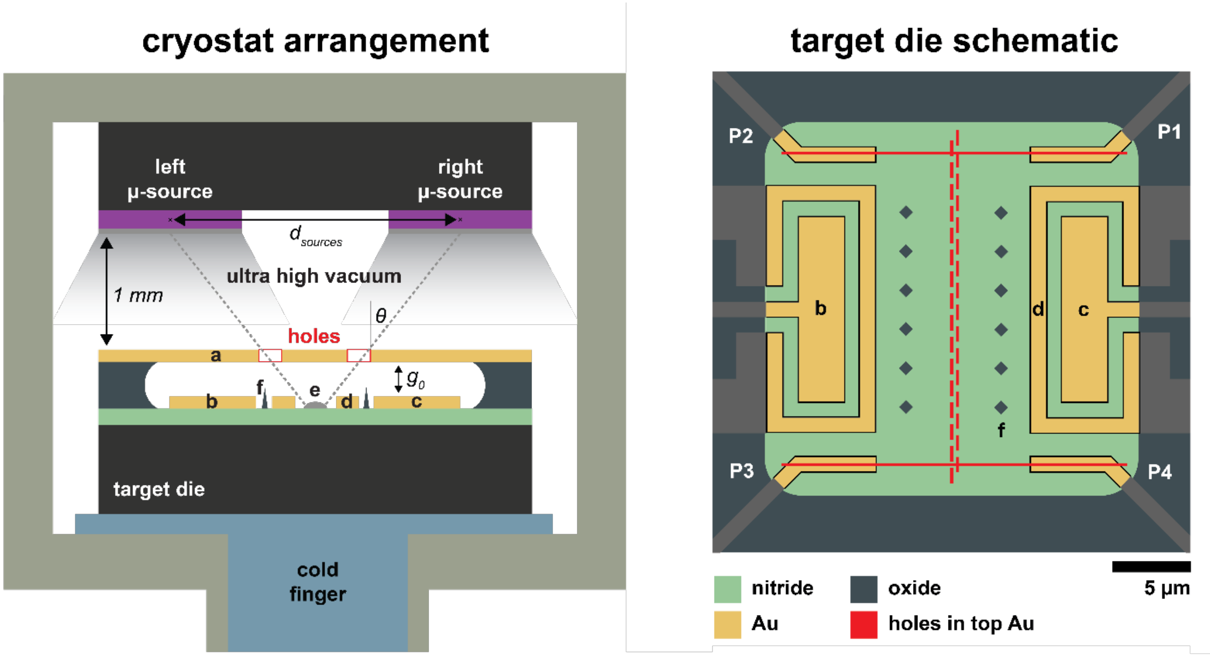

FIGURE 3

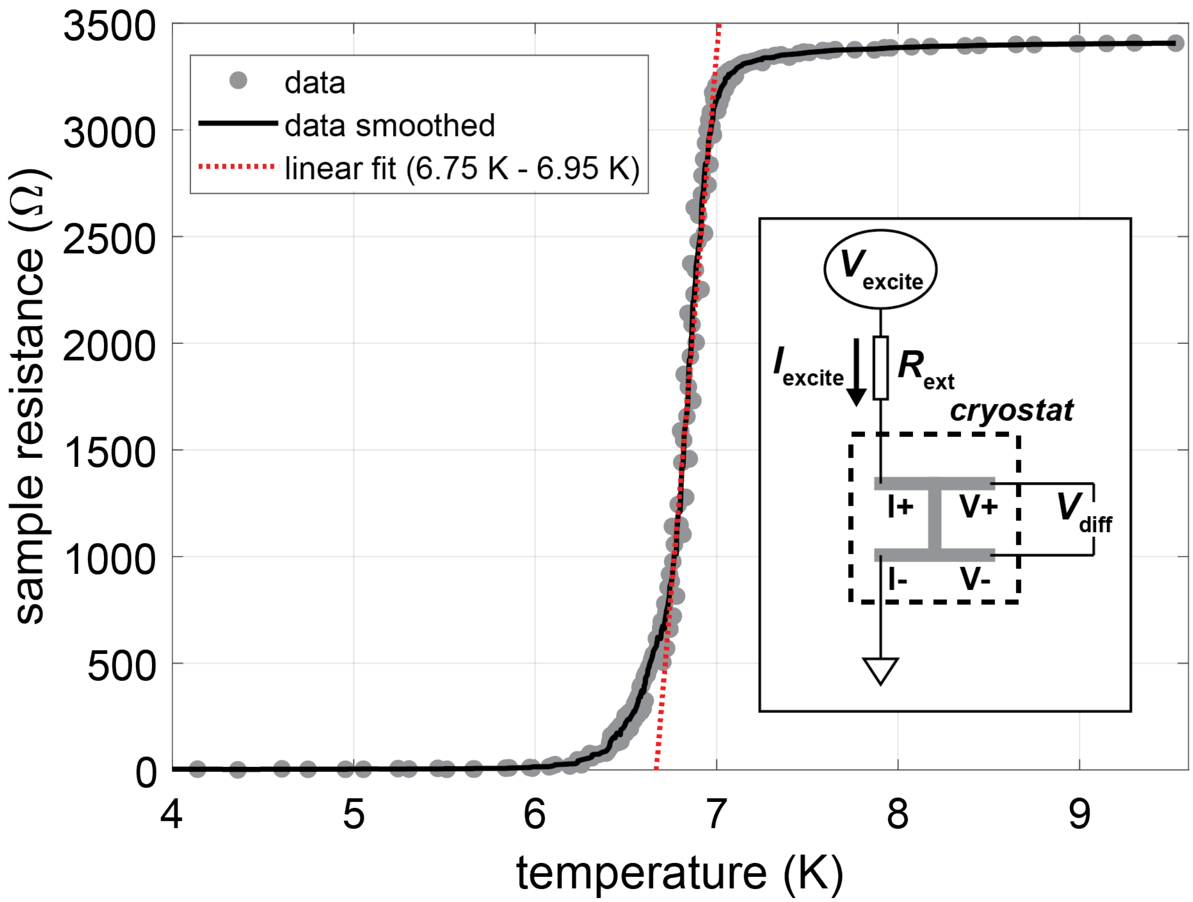

FIGURE 4

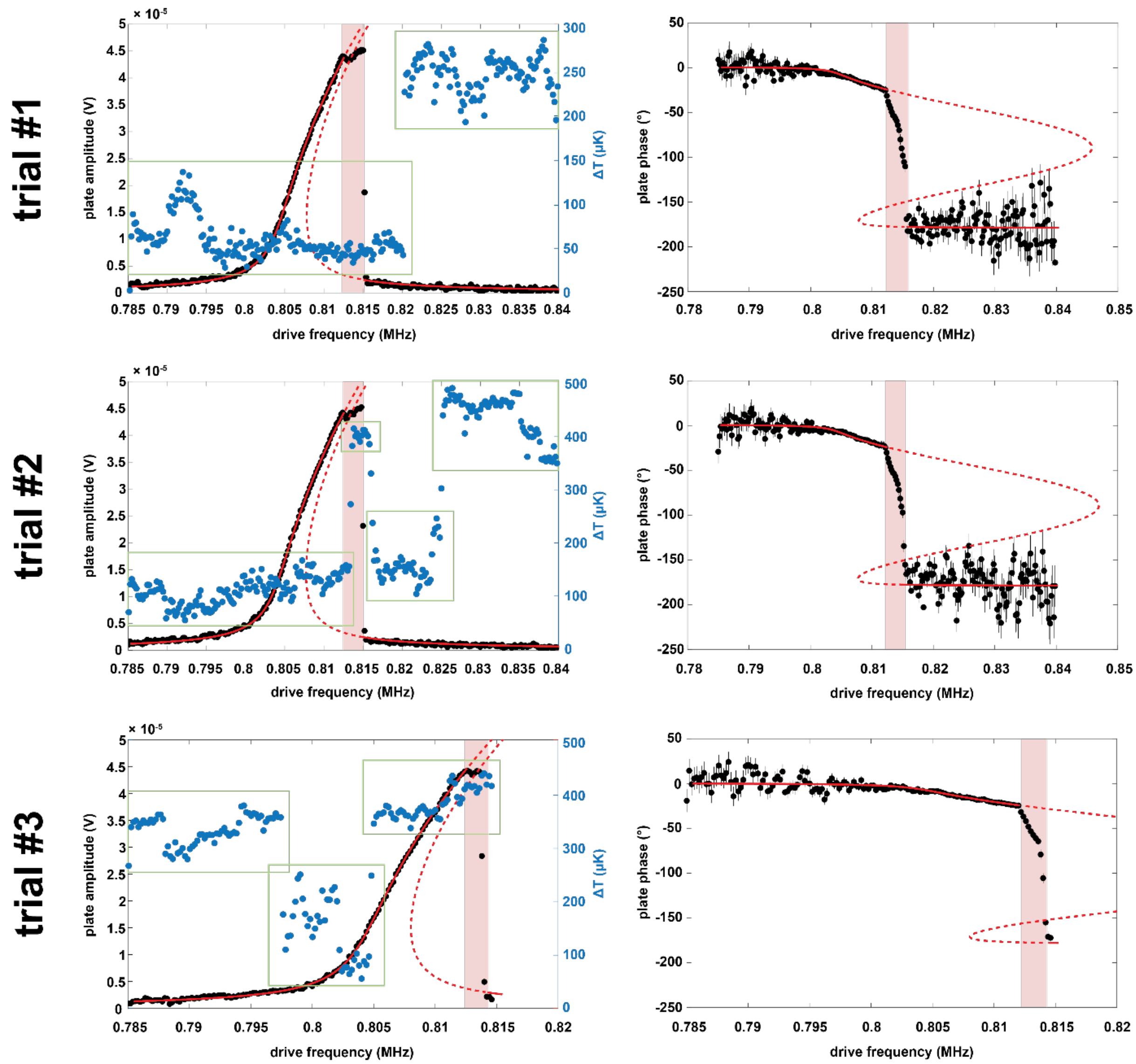

trial #1
trial #2
trial #3
plate amplitude (V)
× 10⁻⁵
ΔT (µK)
drive frequency (MHz)
plate phase (°)

FIGURE 5

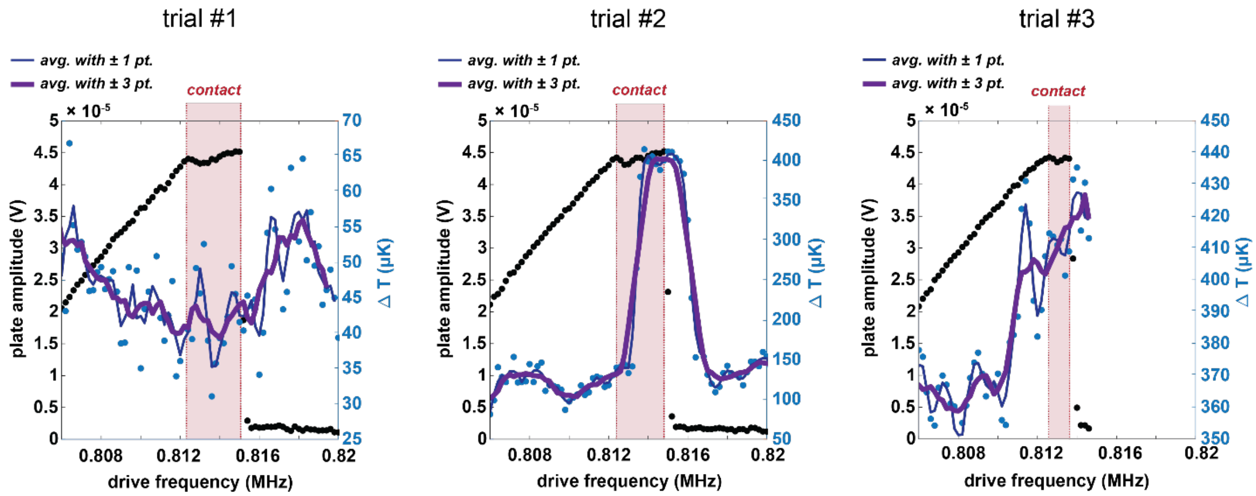

FIGURE 6

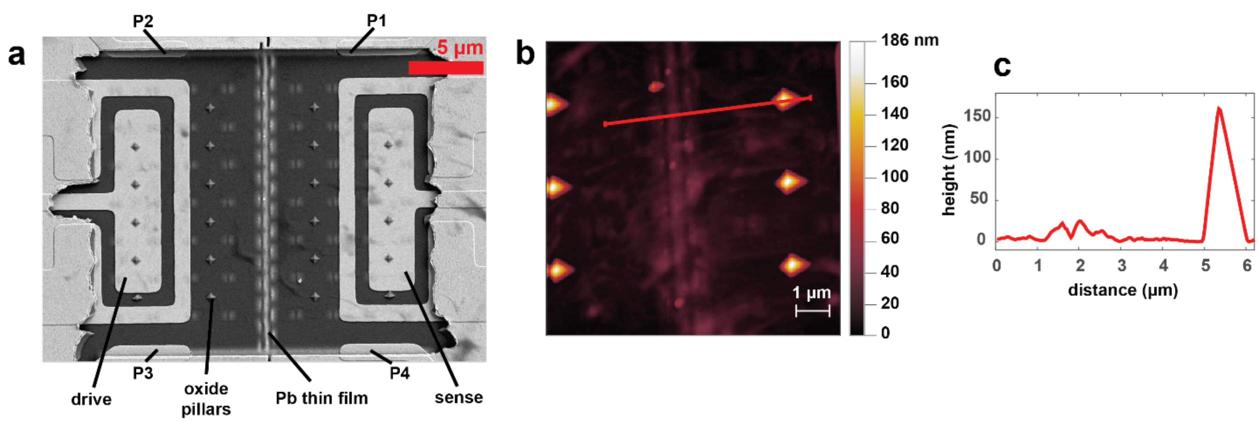

FIGURE 7

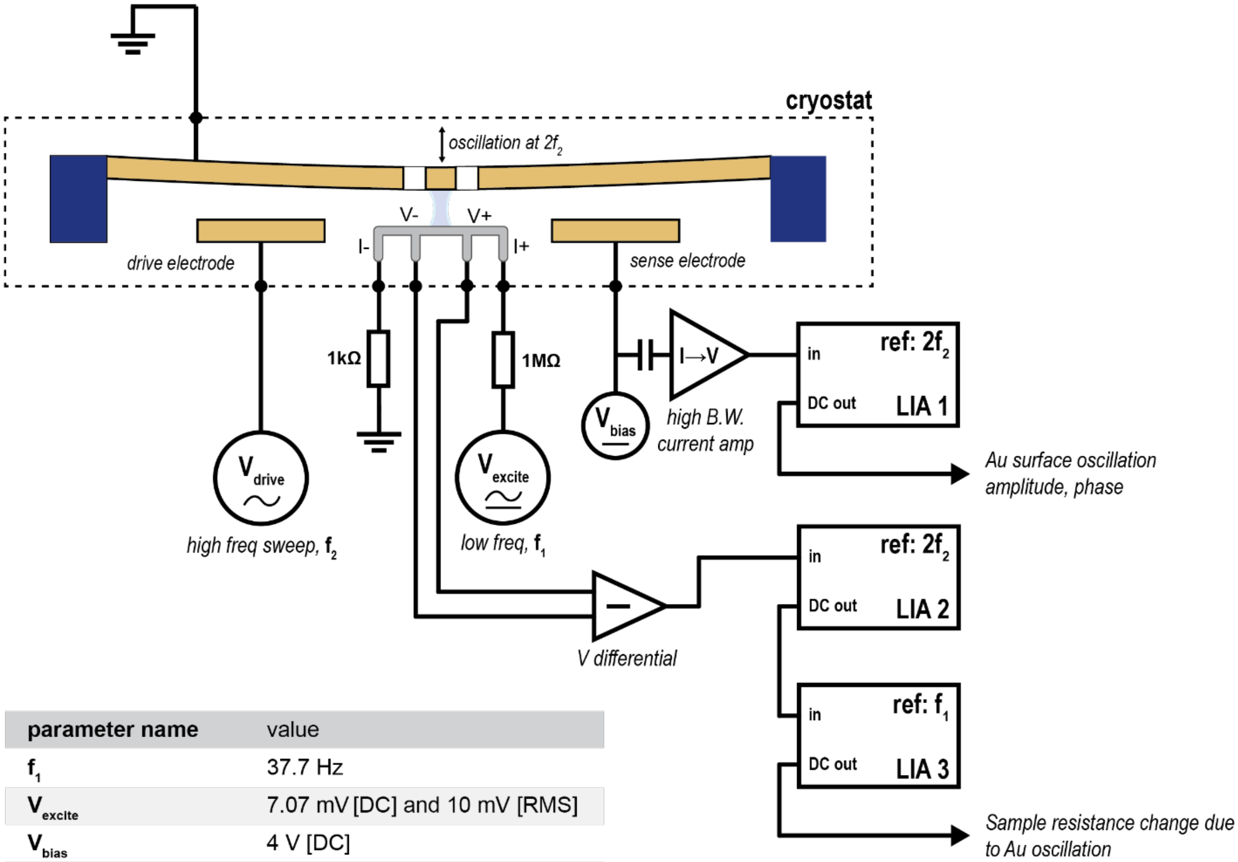

parameter name	value
f_1	37.7 Hz
V_{excite}	7.07 mV [DC] and 10 mV [RMS]
V_{bias}	4 V [DC]
f_2 range	785 kHz to 840 kHz
f_2 frequency step	200 Hz
f_2 time step	90 s
V_{drive}	3 V [RMS]
LIA 1 time constant	30 s
LIA 2 time constant	10 ms
LIA 3 time constant	30 s

FIGURE 8

a

	min. gap	max. gap	avg. gap	L_{10}	L_{25}
Case 1	63 nm	93 nm	85 nm	1.2 μm	4.6 μm
Case 2	73 nm	131 nm	118 nm	0.8 μm	2.0 μm
Case 3	66 nm	169 nm	141 nm	0.5 μm	1.3 μm

b